Enhanced electron correlations in the binary stannide PdSn$_4$: A homologue of the Dirac nodal arc semimetal PtSn$_4$

C. Q. Xu,[1,2] W. Zhou,[1] R. Sankar,[3] X. Z. Xing,[4] Z. X. Shi,[4] Z. D. Han,[1] B. Qian,[1,*] J. H. Wang,[5] Zengwei Zhu,[5]
J. L. Zhang,[6] A. F. Bangura,[7] N. E. Hussey,[8] and Xiaofeng Xu[1,2,†]

[1]*Department of Physics, Advanced Functional Materials Laboratory, Changshu Institute of Technology, Changshu 215500, China*
[2]*Department of Physics, Hangzhou Normal University, Hangzhou 310036, China*
[3]*Center for Condensed Matter Sciences, National Taiwan University, Taipei 10617, Taiwan*
[4]*School of Physics, Key Laboratory of MEMS of the Ministry of Education, Southeast University, Nanjing 211189, China*
[5]*Wuhan National High Magnetic Field Center, School of Physics, Huazhong University of Science and Technology, Wuhan 430074, China*
[6]*High Magnetic Field Laboratory, Chinese Academy of Sciences, Hefei 230031, China*
[7]*Max-Planck-Institut fur Festkorperforschung, Heisenbergstrasse 1, D-70569 Stuttgart, Germany*
[8]*High Field Magnet Laboratory (HFML-EMFL), Radboud University, Toernooiveld 7, 6525ED Nijmegen, Netherlands*

(Received 2 August 2017; published 10 November 2017)

The advent of nodal-line semimetals, i.e., systems in which the conduction and valence bands cross each other along a closed trajectory (line or loop) inside the Brillouin zone, has opened up a new arena for the exploration of topological condensed matter in which, due to a vanishing density of states near the Fermi level, electron correlation effects also may play an important role. Despite this conceptual richness, however, material realization of nodal-line (loop) fermions is rare with PbTaSe$_2$, ZrSiS, and PtSn$_4$ as the only promising known candidates. Here we report the synthesis and physical properties of a semimetal PdSn$_4$ that is isostructural with PtSn$_4$ yet possesses quasiparticles with significantly enhanced effective masses. In addition, PdSn$_4$ displays an unusual polar angular magnetoresistance which, at a certain field orientation, varies linearly with fields up to 55 T. Our paper suggests that, in association with its homologue PtSn$_4$ whose low-lying excitations recently were claimed to possess Dirac nodal arcs, PdSn$_4$ may be a promising candidate in the search for novel topological states with enhanced correlation effects.

I. INTRODUCTION

The quest for quantum materials with diverse symmetry-protected topological states has been a major driver of the field of condensed-matter physics in recent years [1,2]. Due to the advent of Dirac/Weyl semimetals (WSMs), the research interest in topological phenomena now encompasses topological insulators (TIs) and semimetals [3,4]. Three-dimensional topological Dirac or Weyl semimetals are new states of matter that possess a linear band dispersion in the bulk along all three-momentum directions, whose low-energy quasiparticles are the condensed-matter analogues of Dirac and Weyl fermions in relativistic high-energy physics. Many exotic transport behaviors associated with these topological states, such as the chiral anomaly and large linear magnetoresistance (LMR), were identified experimentally soon after their discovery [5–10].

More recently, the focus has shifted towards a new breed of topological materials, namely, the topological nodal-line (or nodal loop) semimetals (NLSMs) in which the Dirac node extends along a curve (or loop) in momentum space, in contrast with the isolated Dirac point node present in TIs and Dirac semimetals [11–17]. Their interest arises primarily from the possibility that the topological aspects of NLSMs may be distinct from those associated with TIs or WSMs [2,18]. It is claimed, for example, that due to the vanishing density of states near the Fermi-level ε_F, screening of the Coulomb interaction is weaker in NLSMs than in conventional metals and remains long ranged [19]. This, coupled with their metallic nature, could make NLSMs more susceptible to various types of order (e.g., superconductivity, magnetism, or charge order), both in the bulk [20] and on the surface [21].

In this article, we report the synthesis and physical characterization of the PdSn$_4$ compound that is isostructural with the Dirac nodal arc semimetal PtSn$_4$ [16,17,22]. Unlike a host of other topological materials that are predicted theoretically first and subsequently verified by experiment, PtSn$_4$ was synthesized many years before its classification as a topological material. Inspired by the observation of an ultrahigh magnetoresistance (MR) in high quality single crystals [16], detailed angle-resolved photoemission spectroscopy (ARPES) studies subsequently revealed a novel topological phase in PtSn$_4$: surface-derived Dirac nodes that formed three open lines (arcs) in reciprocal space, one at the Fermi-level ε_F and the other two at a binding energy of 60 meV [17]. These Dirac nodal arcs are thought to be responsible for the observed ultrahigh MR. It is not yet clear, however, how robust this nodal arc structure in PtSn$_4$ is to variations in the strength of the spin-orbit coupling (SOC) or to the presence of strong electron correlations and how fragile these topological nodal-line fermions are to other instabilities, such as charge-density waves (e.g., as in another NLSM ZrSiS [23]). According to band-structure calculations, the Sn p states in PtSn$_4$ account for most of the density of states at ε_F with only a minor contribution from Pt-derived d bands [16]. Therefore, replacing Pt with the lighter element Pd is not expected to change the band structure nor the Dirac nodal structure significantly.

*njqb@cslg.edu.cn
†xiaofeng.xu@cslg.edu.cn

With this in mind, we have synthesized the single crystals of PdSn$_4$, a sister compound of PtSn$_4$ with a nominally reduced SOC and carried out a comprehensive investigation of its bulk physical properties. A large linear MR $\Delta\rho/\rho$, reaching over $\sim$1300% at 2 K under a 9-T field, has been observed along certain field orientations, contrasting markedly with the quadratic MR observed in PtSn$_4$ [16]. The angular dependence of magnetoresistance (AMR) is found to possess a strong anisotropic structure which is smeared out gradually with increasing T. The temperature under which the symmetry of the AMR undergoes this salient change coincides with the characteristic temperatures where the Hall resistivity, thermoelectric power (TEP), and magnetization also show significant variations, implying either a modification of the Fermi surface with decreasing T or a (partial) gapping of carriers.

In addition, clear de Haas–van Alphen (dHvA) oscillations are revealed in magnetization isotherms. Although the main frequencies are found to be almost identical to those of PtSn$_4$, the effective masses are enhanced by a factor of 3 to 4. These heavier masses are reflected in the enhanced coefficient of the T^2 resistivity, the enhanced electronic specific heat coefficient γ, and the enhanced low-T thermopower. Overall, these findings imply the presence of sizable electron correlations in PdSn$_4$ relative to PtSn$_4$, possibly due to coupling to some form of density wave. Based on these observations, we identify PdSn$_4$ as a candidate material in addition to ZrSiS for hosting novel topological states with strong correlations, an ingredient on which much less attention has been paid thus far in the nascent field of topological physics.

II. EXPERIMENT

Single crystals of PdSn$_4$ were fabricated via self-flux methods. High-purity starting materials Pd (3N, 100 mosh from Alfa Aesar) and Sn (3N, from Aladdin) were mixed thoroughly with a molar ratio of 1:20. This process was handled in a glove box filled with protective argon gas (H$_2$O and O$_2$ contents below 0.1 ppm). Then the mixed materials were sealed in vacuumed quartz tubes (diameter $\phi = 2$ cm). The tubes were heated to 673 K for 3 h in a high-temperature box furnace and kept at this temperature for more than 7 days. After furnace cooling of the tubes to room temperature, bulk ingots were harvested. The redundant tin flux on the surface of the crystals was dissolved in dilute hydrochloric acid. The actual stoichiometric ratio between Pd and Sn has been verified by energy dispersive x-ray spectroscopy (see the Supplemental Material [24]).

Single-crystal x-ray diffraction (XRD) measurements were performed at room temperature using a Rigaku diffractometer with Cu $K\alpha$ radiation and a graphite monochromator. A typical XRD pattern is shown in Fig. S1 of the Supplemental Material [24]. Only the (02l0) peaks were observable, suggesting that the crystallographic b axis is perfectly perpendicular to the surface facet of the crystal. All (02l0) peaks can be well indexed with the orthorhombic ($Ccca$, No. 68) space group, the same structure as PtSn$_4$. The crystal lattice parameter b is estimated as 11.451 ± 0.003 A, slightly larger than that in PtSn$_4$. Specific heat data were obtained using a relaxation method on a Quantum Design (QD) physical property measurement

system (PPMS). Resistivity, magnetoresistivity, and Hall data were measured by a standard four-probe method under various field/current configurations on the PPMS. High-field MR data up to 55 T were obtained from the pulsed magnetic-field laboratory in Wuhan. The Hall measurements were conducted by an orthometric electric-contact configuration, and data antisymmetrization was performed based on reversing the field polarities. For TEP measurements, a chip heater was attached to one end of the sample to generate a temperature gradient which was monitored by a constantan-chromel differential thermocouple, and the thermopower voltage was read out by a nanovoltmeter K2182A from Keithley Instruments. The magnetization data were measured using a QD superconducting quantum interference device magnetometer with fields up to 7 T. High-pressure electrical measurements (data shown in the Supplemental Material [24]) were carried out in the PPMS using a piston cylinder-type pressure cell (type: HPC-33, transmission medium: Daphne 7373) with a pressure up to 2.5 GPa.

III. RESULTS

As shown in Fig. S1 of the Supplemental Material [24], all x-ray diffraction peaks obtained on our single crystals can be indexed with the same orthorhombic ($Ccca$, No. 68) space-group structure as PtSn$_4$ [16]. The crystal structure itself is composed of stacks of Pd atoms sandwiched between two coplanar Sn layers that lie within the ac crystallographic plane. Figure 1(a) shows the characteristic temperature dependence of the resistivity $\rho(T)$ of PdSn$_4$ under various magnetic-fields $H \parallel b$, (i.e., perpendicular to the basal plane). The room-temperature resistivity has a value of $\sim$20 $\mu\Omega$ cm and the (zero-field) residual resistivity ratio [(RRR) = $\rho(300$ K$)/\rho(2$ K$)$] reaches values as high as 100, indicating a high degree of metallicity. From room temperature down to 50 K, $\rho(T)$ follows an approximately linear T dependence. Below 50 K, however, $\rho(T)$ crosses over to a quadratic T dependence, i.e., $\rho(T) = \rho_0 + AT^2$—behavior that is more characteristic of correlated metals than TIs. The coefficient A is estimated as 7×10^{-4} $\mu\Omega^{-1}$ cm^{-1} K^2 [see the inset of Fig. 1(a)], which is a factor of 3 higher than has been reported for PtSn$_4$ [16]. This high degree of metallicity is reflected in the size of the transverse MR which at $T = 2$ K reaches about 660% under 9 T when the field is applied along the crystalline b axis.

The specific heat C of PdSn$_4$ is presented in Fig. 1(b). Overall, $C(T)$ of PdSn$_4$ is very similar to that of PtSn$_4$ [16]. Within the measured temperature range, no signature of a thermodynamic phase transition can be resolved. Through fitting the low-T $C(T)$ data to the formula $C(T) = \gamma T + \beta_3 T^3 + \beta_5 T^5$, the Sommerfeld (electronic) coefficient γ and the harmonic (phonon) term β_3 can be extracted [the upper inset of Fig. 1(b)]. The electronic heat capacity after subtracting the phonon contribution is shown in the lower inset of Fig. 1(b). For PdSn$_4$, we find $\gamma = 7$ mJ mol^{-1} K^{-2}, compared to 4 mJ mol^{-1} K^{-2} for PtSn$_4$. This larger value for γ is consistent with the enhanced A coefficient in the low-T resistivity, suggesting that electron correlation effects are indeed more prominent in PdSn$_4$ than in PtSn$_4$. In many correlated metals, the ratio A/γ^2 [known as the Kadowaki-Woods ratio or (KWR)] is found

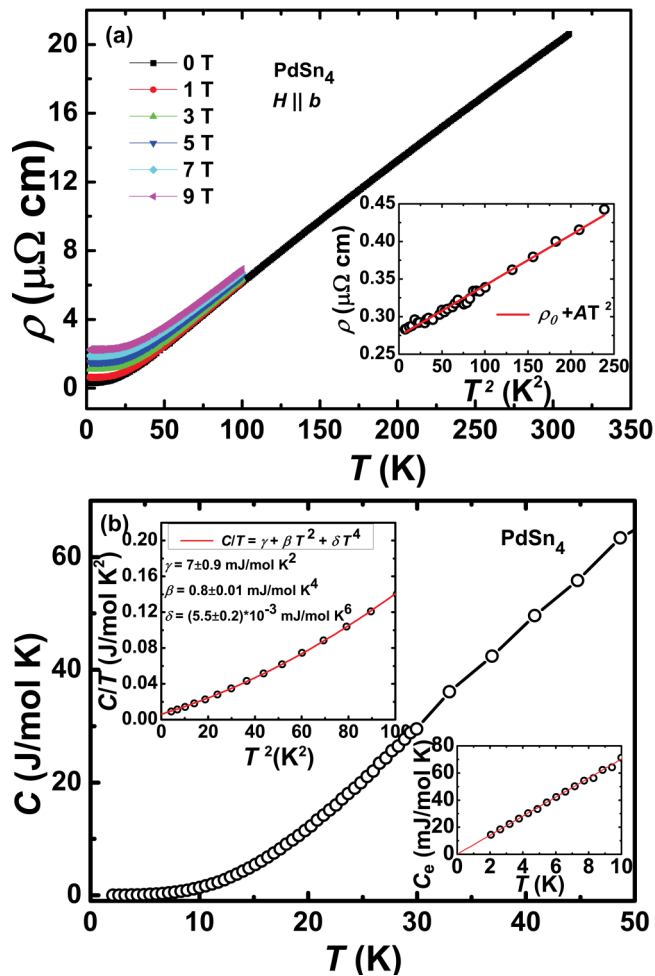FIG. 1. (a) Temperature dependence of resistivity ρ under different magnetic-fields $H \parallel b$. The inset is an enlarged view of $\rho(T)$ in the low-temperature regime and the fit to $\rho(T) = \rho_0 + AT^2$. (b) Temperature dependence of specific heat C. The upper inset shows a fit to $C(T) = \gamma T + \beta_3 T^3 + \beta_5 T^5$, and the lower inset is the electronic specific heat C_e after subtracting the phonon contribution.
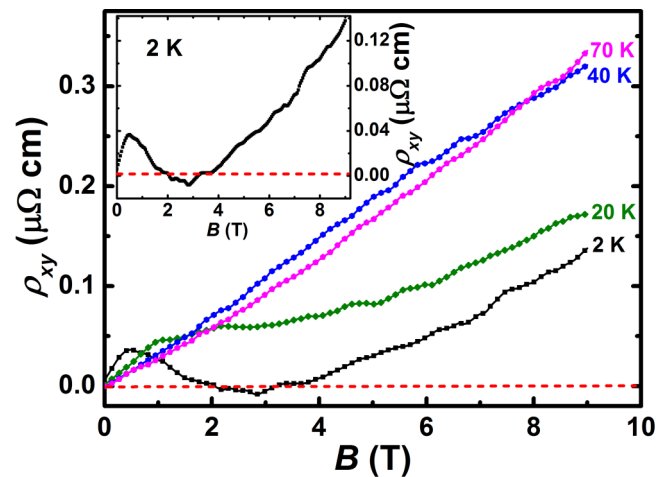

FIG. 2. B dependence of the Hall resistivity ρ_{xy} at different temperatures measured. The inset is an individual plot of $\rho_{xy}(B)$ at $T = 2$ K to highlight the presence of the two inflexion points. The horizontal dashed lines are guides to the eye and demonstrate the negative values in some field interval.

to take a nearly universal value of 10 $\mu\Omega$ cm $(\mathrm{mol}^{-1}\,\mathrm{K}^{-1}\,\mathrm{J})^2$ [25]. For PdSn$_4$, KWR $\sim 14\ \mu\Omega$ cm $(\mathrm{mol}^{-1}\,\mathrm{K}^{-1}\,\mathrm{J})^2$. Whereas this value lies close to the value typically found in strongly correlated electron systems, such as the heavy fermions, it should be noted that the KWR itself is very sensitive to a host of material-specific factors, such as carrier density, multiband effects, and its effective dimensionality [26,27]. Nonetheless, we note that the KWRs in PdSn$_4$ and PtSn$_4$ are comparable in magnitude, implying that any enhancement in A and γ is likely due to correlation effects rather than to differences in their Fermi-surface topologies. Finally, from the coefficient of the T^3 term $\beta_3 = 0.8$ mJ mol^{-1} K^{-4}, we obtain the Debye temperature $\Theta_D \sim 230$ K, similar to the one obtained for PtSn$_4$ (210 K).

The Hall resistivity $\rho_{xy}(B)$ of the PdSn$_4$ single crystal is shown in Fig. 2. At high temperatures, ρ_{xy} is positive and increases linearly with B, implying dominant holelike transport. Below $T \sim 25$ K, however, the $\rho_{xy}(B)$ curve starts to develop nonlinearity and as shown in the inset $\rho_{xy}(B)$ at the lowest temperatures passes through two inflexion points.

This double-inflexion-point structure of the Hall resistivity is a rare phenomenon even in multiband systems. A similar Hall response has been seen, for example, in PdCrO$_2$ where it was ascribed to the anomalous Hall effect induced by antiferromagnetic correlations [28]. It is presumed that in nonmagnetic PdSn$_4$, this peculiar Hall response will have a different origin, although further discussion on this point lies beyond the scope of the present paper.

Figure 3(a) shows the T-dependent TEP over a broad temperature range. As is clear from the figure, magnetic fields appear to have a negligible effect on the TEP, in marked contrast with the large field-dependent TEP found in PtSn$_4$ [16]. This difference, however, may lie in the different carrier mobilities of the two homologues as reflected, for example, in their respective RRRs. Intriguingly, throughout the whole temperature range studied, the TEP of PdSn$_4$ has an opposite sign to the main feature of the Hall resistivity. Such opposite signs between TEP and Hall resistivity have been seen previously in the candidate TI LaAgSb$_2$ [29] as well as in the ferromagnetic superconductor UCoGe [30]. Combined with the highly nonlinear $\rho_{xy}(B)$, this observation suggests a rather complex band structure in PdSn$_4$ near the Fermi level. Upon cooling, the TEP of PdSn$_4$ shows a kink at $T \sim 25$ K, i.e., at the same temperature where the $\rho_{xy}(B)$ curves start to become nonlinear. Perhaps more significantly, the slope of the low-T TEP $S/T = -0.096\ \mu$V/K is found to be approximately one order of magnitude higher than reported in PtSn$_4$ (where, incidentally, the TEP was found to be positive at the lowest temperatures). From this low-T slope, we obtain a corresponding "q" value—linking the TEP to the electronic specific heat via the expression $q = S/T\ (N_{av}e/\gamma)$, here N_{av} is the Avogadro constant—of 1.4, that falls precisely within the range of $0.5 < |q| < 2.0$, found for a host of strongly correlated electron systems [31]. Thus, both the KWR and the q values for PdSn$_4$ appear to be consistent with expectations for correlated metals. We are certainly not aware of other semimetals which give comparable values.
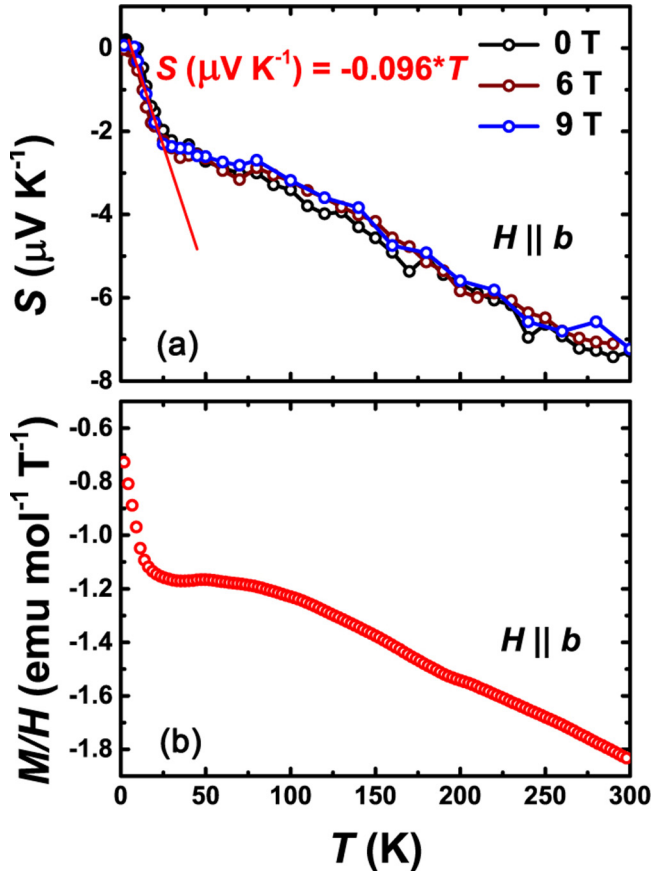
FIG. 3. (a) Temperature dependence of the TEP (S) under magnetic fields of 0, 6, and 9 T ($H \parallel b$). The red solid line is a fit to the Sommerfeld theory of TEP for a single-band metal. (b) Temperature dependence of the magnetic susceptibility ($\chi = M/H$) measured under a field of 0.5 T.

TABLE I. Parameters obtained from dHvA oscillations of a PdSn$_4$ single crystal. F is the peak frequency in the FFT spectra. A_e is the extremal Fermi-surface cross-sectional area calculated from the Onsager relation. m^* and m_e are the effective electron mass and the bare electron mass, respectively. T_D is the Dingle temperature.

dHvA($H \parallel b$)		PdSn$_4$	
Parameter	α	β	γ
F (T)	50	66	125
A_e (Åt^{-2})	4.8×10^{-3}	6.3×10^{-3}	1.2×10^{-2}
m^*/m_e	0.33 ± 0.01	0.41 ± 0.02	0.54 ± 0.01
T_D (K)	10.7 ± 0.5	12.5 ± 1.8	8.3 ± 0.9

in addition to the weak spikes indicated by the asterisks are labeled in sequence as α, β, and γ with corresponding frequencies (F) of 5, 66, and 125 T. These values are very similar to the main frequencies found in PtSn$_4$ [16], suggesting a comparable Fermi-surface topology (at low temperatures). The corresponding areas A_e, obtained from the Onsager relation $F = (\hbar/2\pi e)A_e$, are listed in Table I.

In order to obtain the effective mass m^* for each orbit, the oscillatory dHvA data are fitted at different temperatures to the standard Lifshitz-Kosevich formula [32],

$$\Delta M \propto -R_T R_D \sin\left[2\pi\left(\frac{F}{B} + \frac{1}{2} - \frac{\phi_B}{2\pi} - \delta\right)\right], \quad (1)$$

where $R_T(R_D)$ is the thermal damping factor (Dingle damping factor), ϕ_B is the Berry phase, and δ is an additional phase shift determined by the dimensionality of the Fermi surface (see the Supplemental Material [24] for a discussion of the Berry phase). Therein, $R_T = \frac{2\pi^2 k_B T m^*/eB\hbar}{\sinh(2\pi^2 k_B T m^*/eB\hbar)}$ and $R_D = \exp(2\pi^2 k_B T_D m^*/eB\hbar)$, where k_B is the Boltzmann constant. As shown in Figs. 4(c)–4(e), the best fits for each frequency yield m^* values of 0.33 m_e, 0.41 m_e, and 0.54 m_e for the α, β, and γ pockets, respectively, where m_e is the bare electron mass. The corresponding values for T_D and the effective masses m^* for different bands also are listed in Table I for completeness.

Consistent with the bulk physical properties, the obtained effective masses are found to be significantly larger than in PtSn$_4$ where, for the α, β, and γ pockets (with respective frequencies of 52, 63, and 84 T), the m^* values were all in the range of 0.11–0.16 m_e [16]. Since the mass obtained from dHvA oscillations is equivalent to the thermodynamic mass and proportional to the rate of change in the Fermi-surface area with energy, the fact that the masses are three to four times larger for pockets of the same area implies that the bands near ε_F must be significantly narrower in PdSn$_4$ than in PtSn$_4$. The detailed analysis of the oscillatory signals in the Supplemental Material [24] also provides evidence for a possible nontrivial Berry phase, although verification of the full Dirac-like band structure in PdSn$_4$ will require detailed ARPES studies in due course.

The T-dependent susceptibility, measured under a field of 0.5 T, is shown in Fig. 3(b). Similar to PtSn$_4$, the sample is weakly diamagnetic. Around $T = 25$ K, the susceptibility undergoes a rapid increase. Intriguingly, the whole shape of the $M(T)$ curve exhibits a similar profile to that of TEP, suggesting that the same electrons, which participate in the entropy transport, are responsible for the magnetization. It is worth noting too that the characteristic temperatures (~ 25 K) identified from the abnormal changes in the T-dependent $\rho_{xy}(B)$, TEP, and susceptibility coincide with the temperature at which the symmetry of the AMR, to be discussed in more detail below, also changes, signifying a possible change in the Fermi-surface topology across this temperature. Unfortunately, comparison of the absolute magnitude of the Pauli susceptibility χ_P with PtSn$_4$ is not possible until the additional orbital and van Vleck contributions in both systems are determined independently and subtracted.

The magnetization curves also exhibit clear dHvA oscillations [see Fig. 4(a)], which can provide, in principle, a direct measure of the quasiparticle effective masses for the different bands in PdSn$_4$.

A FFT of the dHvA oscillations is shown in Fig. 4(b). Several independent frequencies are identified, corresponding to different extremal Fermi-surface cross-sectional areas A_e within the Brillouin zone. The three most prominent peaks

Finally, we turn to discuss the anomalous AMR of PdSn$_4$. The AMR measured on a second sample (with RRR ~ 87) under two distinct B-rotation configurations are represented in Figs. 5 and S4 in the Supplemental Material [24], respectively. For the first rotation configuration [referred to as $B \parallel bI$ and depicted schematically in Fig. 5(a)], the field is rotated from
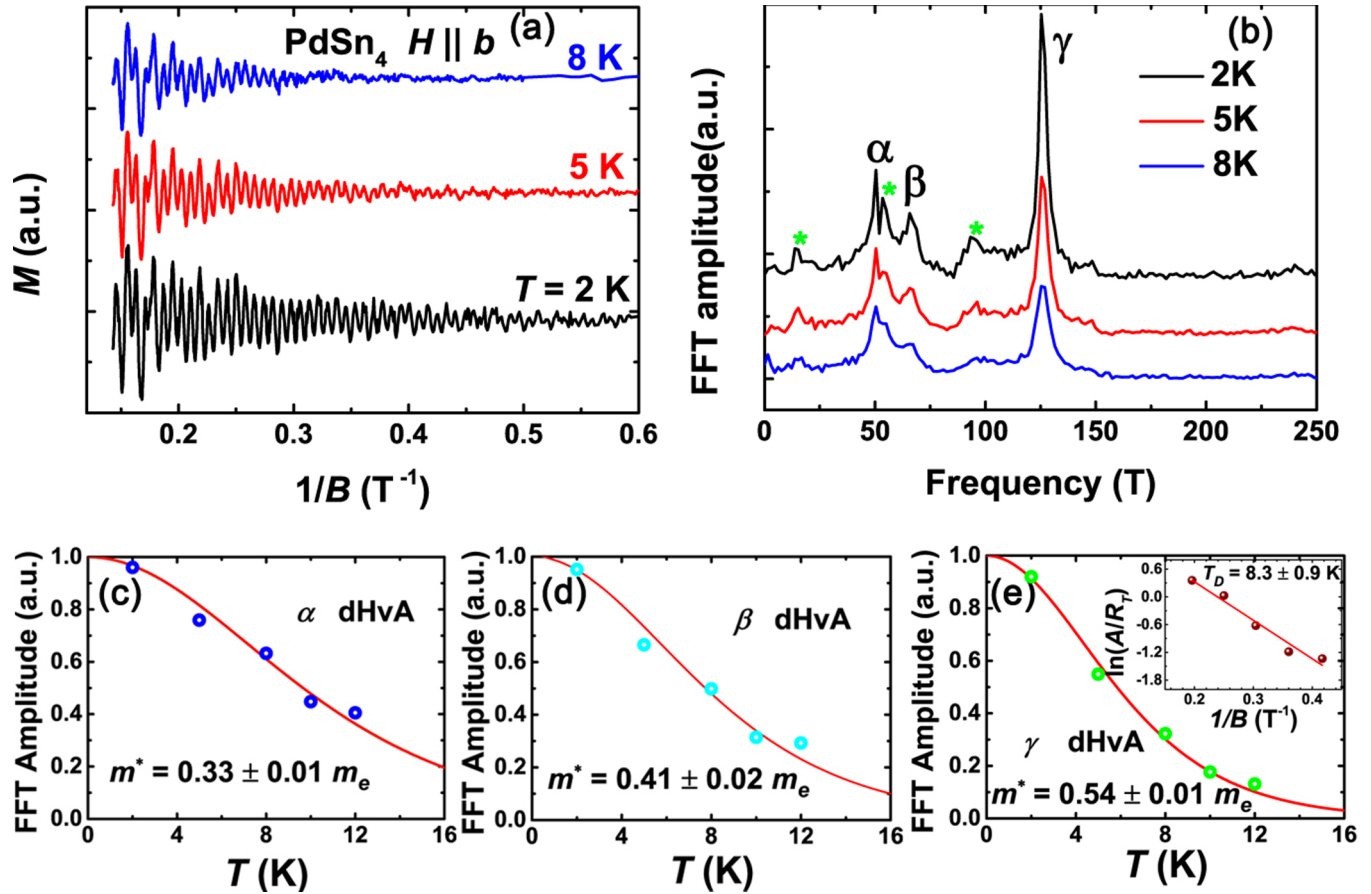
FIG. 4. (a) dHvA oscillations in magnetization at different temperatures (as labeled) after subtracting a polynomial background. The magnetic field is applied along the b axis. (b) Fast Fourier-transform (FFT) spectra of the dHvA data at the same temperatures. At least three extremal Fermi-surface cross-sectional areas are identified by the peaks in the FFT spectra, i.e., α(50 T), β(66 T), and γ(125 T). The other weak peaks are marked by the green asterisks. (c)–(e) Temperature dependence of the normalized FFT amplitude which is proportional to the thermal damping factor R_T. The red solid lines are fits to $R_T = \frac{2\pi^2 k_B T m^*/e B \hbar}{\sinh(2\pi^2 k_B T m^*/e B \hbar)}$, which is used to extract the cyclotron effective mass m^*. In the fitting, B is the effective magnetic field determined by $\frac{1}{B} = \frac{1}{2}[\frac{1}{B_{\min}} + \frac{1}{B_{\max}}]$, where $B_{\min}$ and $B_{\max}$ are the minimum and maximum field values of the FFT region. The inset in (e) shows a typical Dingle plot used to obtain the Dingle temperature T_D. The error bars for m^* and T_D are obtained by the standard deviations during the above fits.

the b axis to $B \parallel I$. As seen from the polar plots of the AMR in Figs. 5(b)–5(d), the angle (θ) dependence of the resistivity under a field of 9 T shows a distinct butterflylike shape at low T, implying a strongly anisotropic Fermi surface. The maximum MR is found at a tilted angle of $\theta \sim 20°$. In comparison, at $\theta = 0°$ and $90°$, the MR is relatively small, resulting in the appearance of "two dips." With increasing temperature, these two dips fade away progressively, and above $T \sim 30$ K, the dip at $\theta = 0°$ disappears altogether. The remaining dip at $\theta = 90°$ makes the polar plot of the AMR resemble a dumbbell with twofold symmetry. In addition, the B dependence of the MR for different θ values shows a variety of forms [see Figs. 5(e)–5(n)]. When $\theta \sim 20°$, i.e., the peak angle in the AMR, the MR grows linearly with B from an almost zero field to the highest field studied (55 T) as shown in Fig. 5(h). On the other hand, when θ is aligned with the dip positions, the MR exhibits downward curvature at low fields while the overall shape remains quite linear. With increasing T, this downward curvature is replaced gradually by the more conventional quadratic low-B MR. The size of the MR at 9 T also is suppressed quickly with increasing T, consistent with

the above $\rho(T)$ measurements under different fields in Fig. 1 (corresponding to $\theta = 0°$).

For the other B-rotation configuration, which we denote as $B \perp I$, meaning that the field remains on the plane perpendicular to the current (see Fig. S4(a) of the Supplemental Material [24]), the AMR evolves with T in the same fashion (see Figs. S4(b)–S4(d) of the Supplemental Material [24]). One difference, however, is that the maximum MR occurs at an angle close to $45°$. The AMR symmetry at 2 K is almost fourfold. In addition, the critical temperature at which the dip at $\theta = 0°$ disappears shifts to ~ 40–50 K, which is slightly higher than the first configuration. As to the B dependence of the MR (see Figs. S4(e)–S4(k) of the Supplemental Material [24]), a linear-in-B MR also is resolved when the field is anchored to the maximum angle ($\theta = 45°$). With increasing T, the quadratic MR at low B is restored gradually while the high-B MR remains linear.

Very similar butterfly AMR has been reported in the NLSM ZrSiS in which the Dirac nodes emerge in both the bulk and the surface electronic states [11,33], in analogy with the Dirac node arc compound PtSn$_4$. In ZrSiS, the butterflylike AMR was
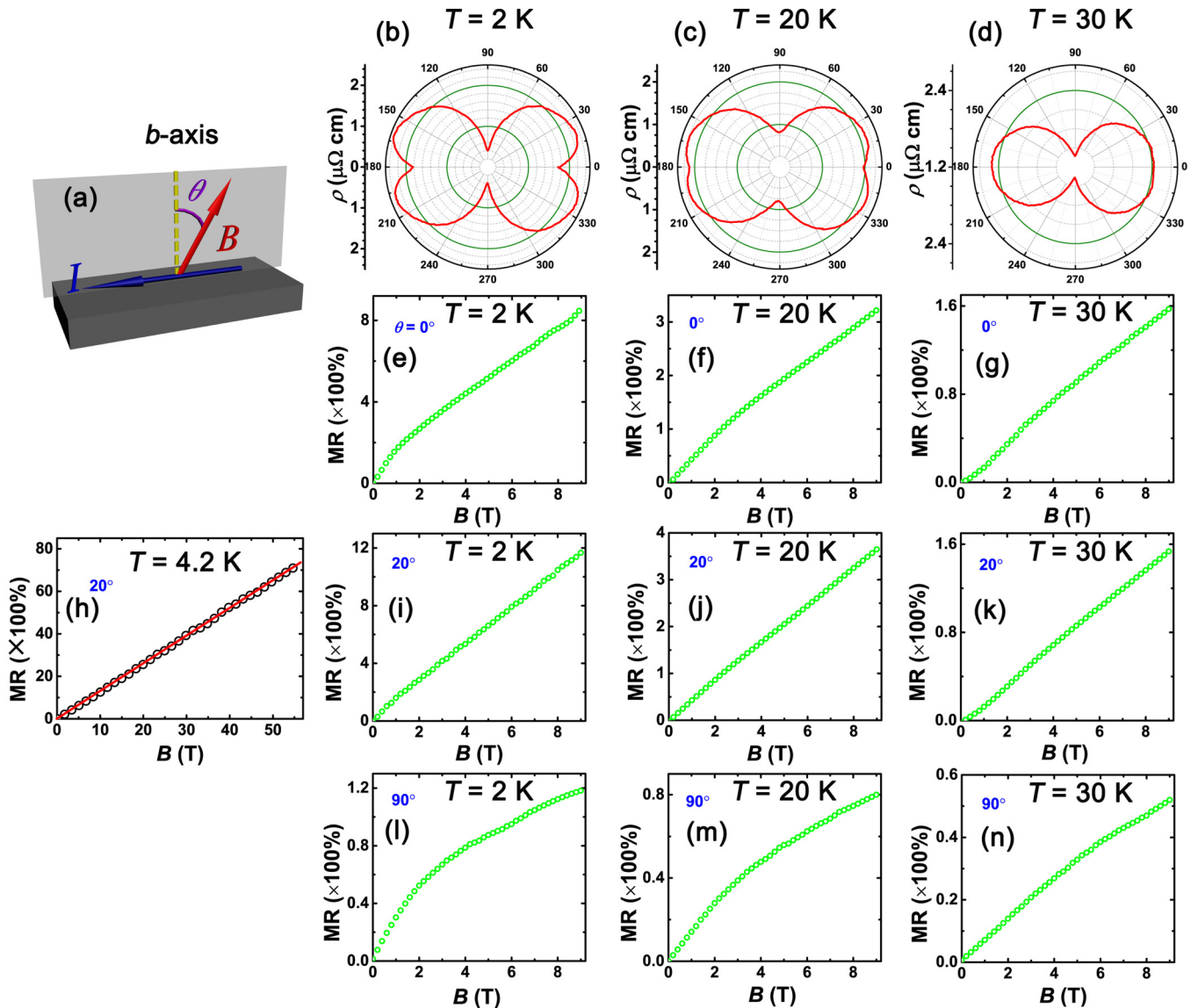
FIG. 5. (a) Schematic of the field/current configurations. The field is constrained to a plane formed by the current flow direction and the crystalline b axis. $\theta = 0°$ corresponds to the $B \parallel b$ axis. (b)–(d) Angle dependence of resistivity ρ under $B = 9$ T for $T = 2$, $T = 20$, and $T = 30$ K, respectively. (e)–(n) Field dependence of MR $= \{[\rho(B) - \rho(0)]/\rho(0)\}$ at angles and temperatures specified in the individual figures. (h) MR measured under a pulsed magnetic field up to 55 T at $\theta = 20°$, $T = 4.2$ K. The red solid line is a guide for the linear B dependence of MR.

disassembled into twofold and fourfold components whose weights both varied with T and B [11]. The butterflylike AMR in ZrSiS persists up to $T = 70$ K, although no butterfly-to-dumbbell change in the AMR is observed.

IV. DISCUSSION

From this study of the bulk transport and thermodynamic properties of single-crystalline PdSn$_4$, a consistent picture for the electronic states near ε_F has emerged. The A coefficient of the T^2 resistivity, the electronic specific heat coefficient γ, and the slope of the TEP in the low-T limit all show significant enhancements relative to the values reported previously in the isostructural Dirac nodal arc semimetal PtSn$_4$. Such enhancement typically is attributed to heavier quasiparticle masses, a hypothesis seemingly confirmed by the observation

of dHvA oscillation frequencies with corresponding m^* values that are on average three to four times larger than those obtained in PtSn$_4$.

The origin of this mass enhancement is currently unknown. However, in nodal-line semimetals, in general, it has been argued [19,20] that the specific properties of the band dispersions near ε_F, in particular, the presence of the Dirac nodal line running parallel to the Fermi surface, can give rise to a Coulomb interaction, both on site or nearest neighbor, that remains partially unscreened. This residual Coulomb interaction can in turn lead to an *enhancement* in m^* rather than a reduction (as seen, for example, at the isolated Dirac points in graphene [34,35]) as well as to an increased tendency towards magnetic or charge-density-wave (CDW) order either in the bulk or on the surface [20,21]. The marked changes in TEP, $M(T)$, the AMR, and $\rho_{xy}(B)$ around 25 K all suggest

changes to sections of the Fermi surface, although clearly further work will be required to elucidate the origin of these features.

The strictly linear MR up to 55 T observed in PdSn$_4$ at certain field angles is another key finding of this paper and contrasts markedly with the quadratic MR seen in its sister PtSn$_4$. A natural question arises concerning the origin of this large LMR. Indeed, the weakly diamagnetic response in nonmagnetic PdSn$_4$ would appear to rule out quantum electron-electron (*e-e*) interference effects as proposed for the origin of the LMR in certain (geometrically constrained) ferromagnets [36,37].

Density fluctuations also have been proposed as the origin of a linear MR, this time in ultrahigh mobility GaAs quantum wells [38]. Such density fluctuations cause a gradient of the Hall voltage (which is linear in B) that will dominate the MR response and give rise to a LMR. However, this situation is unlikely to be applicable here because of the nonlinear Hall resistivity ρ_{xy} at low temperatures in this high-quality PdSn$_4$.

Another possible interpretation of the LMR is the breakdown of weak-field magnetotransport near a quantum critical point [39]. At the critical point for a density-wave transition, for example, the weak-field regime of magnetotransport can collapse to zero with the size of the gap [39]. Indeed, in certain quantum materials exhibiting CDW or spin-density wave (SDW), e.g., LaAgSb$_2$ [29], Ca$_3$Ru$_2$O$_7$ [39], and the iron-based superconductors BaFe$_2$As$_2$ [40] and S-doped FeSe [41], the LMR disappears at or above the CDW or SDW onset temperatures.

In TIs or topological semimetals (TSMs), a LMR can result from a linear-energy dispersion of the Dirac fermions [5,6,42,43]. There, the energy splitting between the lowest and the first Landau level (LL) can be described by $\Delta_{LL} = v_F(2e\hbar B)^{0.5}$. In the quantum limit, Δ_{LL} is much larger than both ε_F and $k_B T$, and as such, all carriers are degenerate in the lowest LL. Thus, once above a certain critical-field B_c, quantum transport will dominate, and a nonsaturating LMR is expected. In this case, a crossover from the low-B quadratic dependence to the high-B linear MR will occur at a specific field strength B_c which follows the T-dependent relation [29]: $B_c = \frac{1}{2e\hbar v_F^2}(\varepsilon_F + k_B T)^2$. Although neither the low-B quadratic MR nor the above T dependence of B_c are seen experimentally, the butterfly AMR observed here for PdSn$_4$ also has been seen in the NLSM ZrSiS, and a LMR without quadratic B dependence at low fields has been reported in other TSMs in which Dirac states firmly were established [6,43–46]. We therefore tentatively attribute the LMR seen here to the existence of a Dirac-like linear dispersion in PdSn$_4$ too.

The change in the AMR symmetry with varying T points to changes in the relative mobilities of different sections of the Fermi surface. The similarity in the dHvA frequencies found for both systems implies that the main features of the Fermi surface remain intact upon Pd substitution. It is nonetheless intriguing that the effective masses are enhanced significantly in PdSn$_4$ by a factor of 3 or 4 compared to PtSn$_4$. Enhancement by such a large factor would appear to rule out electron-phonon coupling as the responsible interaction and instead imply the presence of enhanced electron-electron correlations. These interesting many-body interactions, which have been ignored in most treatments of topological physics to date, certainly deserve more investigation, both theoretically and experimentally. Overall, our collective results suggest that PdSn$_4$ may be a new candidate topological material and a promising platform to study both Dirac physics and correlation effects in a single system.

[1] M. Z. Hasan and C. L. Kane, Topological insulators, Rev. Mod. Phys. **82**, 3045 (2010).

[2] A. A. Burkov, Topological semimetals, Nat. Mater. **15**, 1145 (2016).

[3] Z. Wang, H. Weng, Q. Wu, X. Dai, and Z. Fang, Three-dimensional Dirac semimetal and quantum transport in Cd$_3$As$_2$, Phys. Rev. B **88**, 125427 (2013).

[4] S.-Y. Xu *et al.*, Observation of Fermi arc surface states in a topological semimetal, Science **347**, 294 (2015).

[5] J. Xiong *et al.*, Evidence for the chiral anomaly in the Dirac semimetal Na$_3$Bi, Science **350**, 413 (2015).

[6] D.-X. Qu *et al.*, Quantum oscillations and Hall anomaly of surface states in the topological insulator Bi$_2$Te$_3$, Science **329**, 821 (2010).

[7] X. Huang *et al.*, Observation of the Chiral-Anomaly-Induced Negative Magnetoresistance in 3D Weyl Semimetal TaAs, Phys. Rev. X **5**, 031023 (2015).

[8] C. Shekhar *et al.*, Extremely large magnetoresistance and ultrahigh mobility in the topological Weyl semimetal candidate NbP, Nat. Phys. **11**, 645 (2015).

[9] F. F. Tafti *et al.*, Resistivity plateau and extreme magnetoresistance in LaSb, Nat. Phys. **12**, 272 (2015).

[10] N. Kumar, C. Shekhar, S.-C. Wu, I. Leermakers, O. Young, U. Zeitler, B. Yan, and C. Felser, Observation of pseudo-two-dimensional electron transport in the rock salt-type topological semimetal LaBi, Phys. Rev. B **93**, 241106(R) (2016).

[11] M. N. Ali *et al.*, Butterfly magnetoresistance, quasi-2D Dirac Fermi surface and topological phase transition in ZrSiS, Sci. Adv. **2**, e1601742 (2016).

[12] L. M. Schoop *et al.*, Dirac cone protected by non-symmorphic symmetry and three-dimensional Dirac line node in ZrSiS, Nat. Commun. **7**, 11696 (2016).

[13] J. Hu *et al.*, Evidence of Topological Nodal-Line Fermions in ZrSiSe and ZrSiTe, Phys. Rev. Lett. **117**, 016602 (2016).

[14] M. N. Ali, Q. D. Gibson, T. Klimczuk, and R. J. Cava, Non-centrosymmetric superconductor with a bulk three dimensional Dirac cone gapped by strong spin-orbit coupling, Phys. Rev. B **89**, 020505(R) (2014).

[15] G. Bian *et al.*, Topological nodal-line fermions in spin-orbit metal PbTaSe$_2$, Nat. Commun. **7**, 10556 (2016).

[16] E. Mun, H. Ko, G. J. Miller, G. D. Samolyuk, S. L. Bud'ko, and P. C. Canfield, Magnetic field effects on transport properties of PtSn$_4$, Phys. Rev. B **85**, 035135 (2012).

[17] Y. Wu *et al.*, Dirac node arcs in PtSn$_4$, Nat. Phys. **12**, 667 (2016).

[18] C. Fang *et al.*, Topological nodal line semimetals, Chin. Phys. B **25**, 117106 (2016).

[19] Y. Huh, E.-G. Moon, and Y. B. Kim, Long-range Coulomb interaction in nodal-ring semimetals, Phys. Rev. B **93**, 035138 (2016).

[20] B. Roy, Interacting nodal-line semimetal: Proximity effect and spontaneous symmetry breaking, Phys. Rev. B **96**, 041113(R) (2017).

[21] J. Liu and L. Balents, Correlation and transport phenomena in topological nodal-loop semimetals, Phys. Rev. B **95**, 075426 (2017).

[22] J. Nylén *et al.*, Structural relationships, phase stability and bonding of compounds PdSn$_n$ ($n = 2–4$), Solid State Sci. **6**, 147 (2004).

[23] S. Pezzini, M. R. van Delft, L. Schoop, B. Lotsch, A. Carrington, M. I. Katsnelson, N. E. Hussey, and S. Wiedmann, Unconventional mass enhancement around the Dirac nodal loop in ZrSiS, arXiv:1701.09119, Nat. Phys. (to be published, 2017).

[24] See Supplemental Material at http://link.aps.org/supplemental/10.1103/PhysRevMaterials.1.064201 for the sample characterizations, Hall coefficient, Berry phase, AMR on the second configuration, and the pressure dependence.

[25] K. Kadowaki and S. B. Woods, Universal relationship of the resistivity and specific heat in heavy-Fermion compounds, Solid State Commun. **58**, 507 (1986).

[26] A. C. Jacko *et al.*, A unified explanation of the Kadowaki-Woods ratio in strongly correlated metals, Nat. Phys. **5**, 422 (2009).

[27] N. E. Hussey, Non-generality of the Kadowaki-Woods ratio in correlated oxides, J. Phys. Soc. Jpn. **74**, 1107 (2005).

[28] J. M. Ok, Y. J. Jo, K. Kim, T. Shishidou, E. S. Choi, H.-J. Noh, T. Oguchi, B. I. Min, and J. S. Kim, Quantum Oscillations of the Metallic Triangular-Lattice Antiferromagnet PdCrO$_2$, Phys. Rev. Lett. **111**, 176405 (2013).

[29] K. Wang and C. Petrovic, Multiband effects and possible Dirac states in LaAgSb$_2$, Phys. Rev. B **86**, 155213 (2012).

[30] G. Bastien, A. Gourgout, D. Aoki, A. Pourret, I. Sheikin, G. Seyfarth, J. Flouquet, and G. Knebel, Lifshitz Transitions in the Ferromagnetic Superconductor UCoGe, Phys. Rev. Lett. **117**, 206401 (2016).

[31] K. Behnia *et al.*, On the thermoelectricity of correlated electrons in the zero-temperature limit, J. Phys.: Condens. Matter **16**, 5187 (2004).

[32] D. Shoenberg, *Magnetic Oscillations in Metals* (Cambridge University Press, Cambridge, UK, 1984).

[33] X. F. Wang *et al.*, Evidence of both surface and bulk Dirac bands and anisotropic nonsaturating magnetoresistance in ZrSiS, Adv. Electron Mater. **2**, 1600228 (2016).

[34] D. C. Elias *et al.*, Dirac cones reshaped by interaction effects in suspended graphene, Nat. Phys. **7**, 701 (2011).

[35] G. L. Yu *et al.*, Interaction phenomena in graphene seen through quantum capacitance, Proc. Natl. Acad. Sci. USA **110**, 3282 (2013).

[36] N. Manyala, Y. Sidis, J. F. DiTusa, G. Aeppli, D. P. Young, and Z. Fisk, Magnetoresistance from quantum interference effects in ferromagnets, Nature (London) **404**, 581 (2000).

[37] A. Gerber, I. Kishon, I. Y. Korenblit, O. Riss, A. Segal, M. Karpovski, and B. Raquet, Linear Positive Magnetoresistance and Quantum Interference in Ferromagnetic Metals, Phys. Rev. Lett. **99**, 027201 (2007).

[38] T. Khouri, U. Zeitler, C. Reichl, W. Wegscheider, N. E. Hussey, S. Wiedmann, and J. C. Maan, Linear Magnetoresistance in a Quasi-Free Two-Dimensional Electron Gas in an Ultrahigh Mobility GaAs Quantum Well, Phys. Rev. Lett. **117**, 256601 (2016).

[39] J. Fenton and A. J. Schofield, Breakdown of Weak-Field Magnetotransport at a Metallic Quantum Critical Point, Phys. Rev. Lett. **95**, 247201 (2005).

[40] K. K. Huynh, Y. Tanabe, and K. Tanigaki, Both Electron and Hole Dirac Cone States in Ba(FeAs)$_2$ Confirmed by Magnetoresistance, Phys. Rev. Lett. **106**, 217004 (2011).

[41] Y. Sun, S. Pyon, and T. Tamegai, Electron carriers with possible Dirac-cone-like dispersion in FeSe$_{1-x}$S$_x$ ($x = 0$ and 0.14) single crystals triggered by structural transition, Phys. Rev. B **93**, 104502 (2016).

[42] X. Z. Xing *et al.*, Large linear magnetoresistance in a transition-metal stannide β-RhSn$_4$, Appl. Phys. Lett. **109**, 122403 (2016).

[43] T. Liang *et al.*, Ultrahigh mobility and giant magnetoresistance in the Dirac semimetal Cd$_3$As$_2$, Nat. Mater. **14**, 280 (2015).

[44] R. Xu *et al.*, Large magnetoresistance in non-magnetic silver chalcogenides, Nature (London) **390**, 57 (1997).

[45] W. Zhang, R. Yu, W. Feng, Y. Yao, H. Weng, X. Dai, and Z. Fang, Topological Aspect and Quantum Magnetoresistance of $\beta-$Ag$_2$Te, Phys. Rev. Lett. **106**, 156808 (2011).

[46] L. P. He, X. C. Hong, J. K. Dong, J. Pan, Z. Zhang, J. Zhang, and S. Y. Li, Quantum Transport Evidence for the Three-Dimensional Dirac Semimetal Phase in Cd$_3$As$_2$, Phys. Rev. Lett. **113**, 246402 (2014).